

# Growth of Uniquely Small Tin Clusters on Highly Oriented Pyrolytic Graphite

Sumit Beniwal, Wenrui Chai, Mengxiong Qiao, Zahra Bajalan, Ali S. Ahsen, Kasala P. Reddy, Yankun Chen, Graeme Henkelman, and Donna A. Chen\*



Cite This: *J. Phys. Chem. C* 2024, 128, 3567–3577



Read Online

ACCESS |



Metrics & More

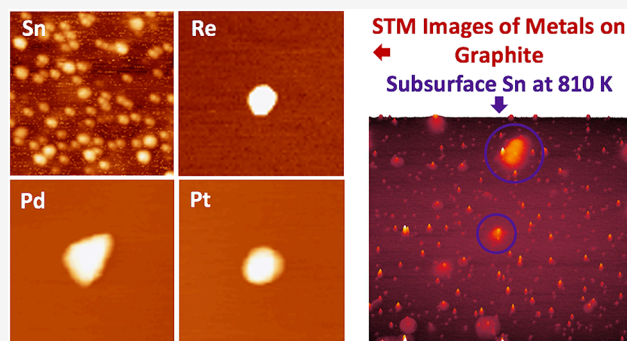


Article Recommendations



Supporting Information

**ABSTRACT:** Sn clusters have been grown on highly oriented pyrolytic graphite (HOPG) surfaces and investigated by scanning tunneling microscopy (STM), X-ray photoelectron spectroscopy (XPS), and density functional theory (DFT) calculations. At low Sn coverages ranging from 0.02 to 0.25 ML, Sn grows as small clusters that nucleate uniformly on the terraces. This behavior is in contrast with the growth of transition metals such as Pd, Pt, and Re on HOPG, given that these metals form large clusters with preferential nucleation for Pd and Pt at the favored low-coordination step edges. XPS experiments show no evidence of Sn–HOPG interactions, and the activation energy barrier for diffusion calculated for Sn on HOPG (0.06 eV) is lower or comparable to those of Pd, Pt, and Re (0.04, 0.22, and 0.61 eV, respectively), indicating that the growth of the Sn clusters is not kinetically limited by diffusion on the surface. DFT calculations of the binding energy/atom as a function of cluster size demonstrate that the energies of the Sn clusters on HOPG are similar to those of Sn atoms in the bulk for Sn clusters larger than 10 atoms, whereas the Pt, Pd, and Re clusters on HOPG have energies that are 1–2 eV higher than in the bulk. Thus, there is no thermodynamic driving force for Sn atoms to form clusters larger than 10 atoms on HOPG, unlike for Pd, Pt, and Re atoms, which minimize their energy by aggregating into larger, more bulk-like clusters. In addition, annealing the Sn/HOPG clusters to 800 and 950 K does not increase the cluster size, but instead removes the larger clusters, while Sn deposition at 810 K induces the appearance of protrusions that are believed to be from subsurface Sn. DFT studies indicate that it is energetically favorable for a Sn atom to exist in the subsurface layer only when it is located at a subsurface vacancy.



## INTRODUCTION

Understanding the growth of Sn-based clusters on surfaces is important for a variety of applications in battery electrodes and microelectronics,<sup>1,2</sup> and in catalysis and electrocatalysis, in which bimetallic Sn–Pt clusters have superior selectivity for the desired products compared to Pt.<sup>3–6</sup> For example, knowledge of the interface between Sn and carbon supports is valuable for applications involving the Sn-carbon nanocomposites used in the anodes of Li ion batteries.<sup>2,7–10</sup> Metallic Sn anodes have a high Li ion storage capacity, but are mechanically unstable due to the large volume expansion during lithiation.<sup>2,7,8</sup> However, nanosized Sn particles intercalated into graphite sheets have better stability due to the smaller change in absolute volume, and therefore, these Sn-graphite composites are promising anode materials that can combine the desired properties of high reversible capacity with good stability upon cycling.<sup>7,8,10</sup> Small Sn particles also maximize the contact between the particle and the carbon support and result in superior electrochemical performance.<sup>7</sup>

In general, the growth of metals on HOPG is consistent with high mobility of atoms on the surface and the formation of

thermodynamically favored three-dimensional (3D) clusters.<sup>11–13</sup> Specifically, 3D cluster growth is observed at room temperature for post-transition metals that are neighbors of Sn in the periodic table, such as Ge<sup>14,15</sup> and Sb.<sup>15–18</sup> The growth of 3D islands on HOPG is also reported for many transition metals.<sup>11</sup> Annealing the clusters deposited at room temperature increases the cluster size for Ge<sup>19</sup> as well as for transition metals like Ni,<sup>20</sup> Ru,<sup>21</sup> Cu,<sup>11</sup> Ag,<sup>11</sup> Pt,<sup>11</sup> and Mo.<sup>11</sup> Moreover, decoration of the step edges of HOPG by deposited metals is consistent with the high mobility that allows the atoms to diffuse to the most energetically favored binding sites, as observed for Pt,<sup>12,22–24</sup> Pd,<sup>25</sup> Ru,<sup>21</sup> Ag,<sup>13,26</sup> Cu,<sup>27,28</sup> Ge<sup>14,15,19</sup> Sb,<sup>16–18</sup> and Mo.<sup>29</sup> While metal growth on freshly cleaved (pristine) HOPG yields relatively large clusters, the dispersion

**Received:** December 16, 2023

**Revised:** January 15, 2024

**Accepted:** January 23, 2024

**Published:** February 19, 2024



of metal atoms can be increased by sputtering HOPG with Ar, Ne, or N<sub>2</sub> ions to intentionally create defects, as has been reported for Pd,<sup>25,30–34</sup> Pt<sup>23,24,35</sup> Au,<sup>32,36</sup> Ag,<sup>36</sup> Ru,<sup>21</sup> Fe,<sup>37</sup> and Cs.<sup>38</sup>

Alkali, alkaline earth, and rare earth metals are known to readily intercalate into pristine graphite.<sup>27,39,40</sup> For example, Cs atoms are believed to enter the subsurface region via defects such as the basal plane step edge,<sup>39</sup> and the energy gained from Cs interaction with the graphene sheets offsets the energy required for exfoliation.<sup>38</sup> Although the transition metals and post-transition metals typically do not intercalate into pristine graphite, Thiel and co-workers showed that a number of metals, such as Cu,<sup>27,41,42</sup> Fe,<sup>1,41</sup> Ru,<sup>41–43</sup> Pt,<sup>41</sup> and Dy<sup>41,42</sup> become encapsulated by graphene layers; metal encapsulation requires both high temperature deposition and ion bombardment to create point defects for portals into the subsurface.<sup>41,42</sup> In contrast, Au and Ag do not become encapsulated when deposited at elevated temperature on the ion bombarded HOPG because the interactions of the metals with HOPG are not strong enough to offset the energetic cost of separating the graphene sheets.<sup>44</sup>

Our group's previous studies of Sn on TiO<sub>2</sub>(110) demonstrated that small clusters of Sn were formed due to the strong interaction of Sn with the titania support.<sup>45</sup> Specifically, Sn is oxidized, while titania is reduced at the cluster-support interface. The weak Sn–Sn interaction compared to the Sn-titania interaction results in no thermodynamic driving force for Sn to aggregate into large particles, which is contrary to what is observed for other metals on TiO<sub>2</sub>(110), including Au,<sup>46–48</sup> Cu,<sup>49,50</sup> Pt,<sup>46,51</sup> Ni,<sup>50</sup> Ag,<sup>52</sup> Rh,<sup>51</sup> and Pd.<sup>53</sup> In this work, the nucleation and growth of Sn clusters on highly oriented pyrolytic graphite (HOPG) carbon supports were investigated. Since HOPG is a chemically inert support unlike titania, it was expected that there should be no strong interactions between the support and the metal clusters, and therefore, larger clusters might form. Surprisingly, STM experiments demonstrate that deposition of Sn on HOPG results in very small clusters with a high cluster density, in contrast with the behavior of transition metals such as Pt, Pd, and Re deposited under similar conditions. Furthermore, the deposition of Sn on HOPG at elevated temperatures or after annealing to high temperatures does not produce larger Sn clusters but appears to induce the formation of subsurface Sn.

## ■ EXPERIMENTAL METHODS

Experiments were carried out in two stainless steel ultrahigh vacuum chambers that have been described in detail elsewhere.<sup>54–57</sup> The first chamber ( $P = 1.5 \times 10^{-10}$  Torr) houses an Omicron VT-25 STM, quadrupole mass spectrometer (Leybold-Inficon, Transpector 2), and a single-channel hemispherical analyzer (Omicron EA125) for X-ray photoelectron spectroscopy (XPS).<sup>54,55</sup> The second chamber ( $P = 2 \times 10^{-9}$  Torr) is equipped with a multichannel hemispherical analyzer (Omicron EA2000 SPHERA) for XPS experiments, and a quadrupole mass spectrometer (Stanford Research Systems, RGA 300).<sup>56,57</sup> Both chambers have commercial metal evaporators for Sn deposition (Oxford Applied Research, EGCO4), quartz crystal microbalances for measuring Sn coverages (InficonXTM-2), and load lock chambers for the rapid introduction of samples and STM tips. One monolayer (ML) is defined as the packing density of the: Pt(111) surface ( $1.50 \times 10^{15}$  atoms/cm<sup>2</sup>) for Pt and Sn; Pd(111) surface for Pd ( $1.53 \times 10^{15}$  atoms/cm<sup>2</sup>); and Re(0001) surface for Re

( $1.51 \times 10^{15}$  atoms/cm<sup>2</sup>). The QCM was calibrated by depositing submonolayer coverages of Sn on Pt(111) and Pt on Pt(111) and imaging by STM.<sup>58</sup> The reported surface coverages in ML are based on the flux measured by the QCM, assuming a sticking probability of unity; however, for deposition of these metals on HOPG above room temperature, the sticking probability appears to be <1, as further discussed in the Results section.

HOPG crystals (SPI Supplies, 10 mm × 10 mm × 1 mm) were mounted on an Omicron Ta sample plate and supported with Ta foil straps, as previously described.<sup>59</sup> Samples were heated via electron bombardment from a tungsten filament position directly behind the crystal, and temperatures were measured with an infrared pyrometer, which was calibrated against a type K thermocouple spotwelded to the Ta sample plate.<sup>59,60</sup> Before each STM experiment, the HOPG crystal was cleaved in air using adhesive tape and heated to 950 K for 12 min in UHV before metal deposition; surface cleanliness was confirmed by XPS and STM. For the modified HOPG surfaces, the crystal was sputtered with Ar<sup>+</sup> at 500 eV and 100 nA for 10 s and then annealed at 950 K for 10 min.

Sn was deposited by heating pure Sn pellets (ESPI 99.999%) in a Ta crucible, while Re, Pt, and Pd were deposited from the pure rods (ESPI, 99.99%). All metals were deposited at a rate of 0.035–0.050 ML/min for the STM experiments. For the XPS experiments, the deposition rates for Sn were 0.15–0.26 ML/min, and the HOPG substrate was annealed at 850 K for 3 min after cleaving and before deposition.

STM experiments were carried out with electrochemically etched tungsten tips<sup>45,61</sup> with typical sample biases ranging from +1.4–2.5 V and tunneling currents of 0.01–0.05 nA. XPS data were collected with a Mg K<sub>α</sub> source and step size of 0.01 eV using a dwell time of 0.6 s for 0.25 ML Sn at room temperature and 2–3 s for 0.005 ML Sn and 0.25 ML Sn deposited at 810 K.

Cluster heights were measured for all clusters in the image using an in-house program that has been described in detail elsewhere,<sup>62,63</sup> and the number of clusters/image were counted manually. For the higher coverages of Sn deposited at room temperature (0.05 and 0.25 ML), automated height analysis was not possible, and therefore, cluster heights and diameters were determined manually using the WSxM Image shareware program. Reported cluster diameters were also measured with WSxM Image, and STM images were plane-flattened and deglitched using WSxM Image.

## ■ COMPUTATIONAL METHODS

DFT calculations were conducted as implemented in the Vienna Ab Initio Simulation Package.<sup>64–68</sup> Core electrons were described within the projected augmented wave framework, while valence electrons were described with a plane wave basis set up to an energy cutoff of 400 eV.<sup>69</sup> The generalized gradient approximation in the form of the Perdew, Burke, and Ernzerhof functional was used to model electronic exchange and correlation,<sup>70</sup> and van der Waals interactions were calculated using the DFT-D2 method.<sup>71</sup> For all calculations, the Brillouin zone integration was carried out at the gamma point. Spin polarization was used in all calculations. The HOPG structure was modeled with a (6 × 9 × 1) supercell. Binding energies of metal clusters were calculated using their bulk states as the energy reference according to the equation below:

$$E_{\text{BE}} = E_{\text{cluster}^*} - E_{\text{surface}} - nE_{\text{metal}}$$

where  $E_{\text{BE}}$  is binding energy,  $E_{\text{cluster}^*}$  is the energy of the cluster and support,  $E_{\text{surface}}$  is the energy of the supporting surface alone,  $n$  is the number of metal atoms in the cluster, and  $E_{\text{metal}}$  is the energy of a metal atom in the bulk state. These binding energies were determined using a single layer of HOPG, given that additional graphite layers have a negligible effect on the binding energy. Structures of the metal clusters up to a size of five atoms were sampled to find the lowest energy structure; sampled geometries included all linear, convex polygon, and convex polyhedron structures. Clusters of larger sizes up to 15 atoms were created by adding an atom to a stable structure in positions that maximize the number of metal–metal bonds. Binding energies of metal clusters in the sublayer were calculated using two layers of HOPG, and the optimized structures of all subsurface clusters were a single layer high. The term “pristine” HOPG means that there were no vacancy defects in the surface or subsurface layers. Reaction pathways and energy barriers were determined using the climbing image nudged elastic band method.<sup>72</sup>

Simulated STM images were created from isosurfaces of the total electron density. The simulated line profiles were generated using a tip diameter of 30 Å; this estimated value was based on the fact that the smallest cluster diameters measured in the STM images were 20–30 Å and assumed to be limited by tip convolution effects.<sup>61,73</sup> No convolution was included for the simulated STM images.

## RESULTS

STM images show that the freshly cleaved HOPG surface before metal deposition consists of atomically flat terraces ~400–1000 Å wide separated by single-layer steps that are 3.4 Å high (Figure 1a). After deposition of 0.02 ML of Sn (1 ML =  $1.5 \times 10^{15}$  atoms/cm<sup>2</sup>), many small clusters appear with an average height of  $2.7 \pm 1.2$  Å, which corresponds to clusters

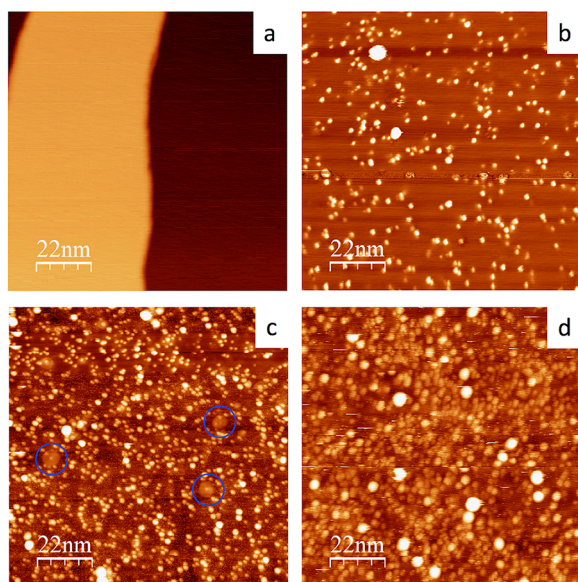


**Figure 1.** STM images for (a) freshly cleaved HOPG; and the following coverages of Sn on HOPG deposited at room temperature: (b) 0.02 ML; (c) 0.05 ML; and (d) 0.25 ML. The blue circles in (c) indicate bubble-like features that could be associated with subsurface Sn.

**Table 1.** Average Heights and Cluster Densities for Metals on HOPG

Surface	Avg. height (Å)	Cluster density (cm <sup>-2</sup> )
0.02 ML Sn	2.7 ± 1.2	2.96 × 10 <sup>12</sup>
0.05 ML Sn	3.5 ± 1.0	8.60 × 10 <sup>12</sup>
0.05 ML Sn, anneal 800 K 3 min	2.8 ± 1.1	9.54 × 10 <sup>12</sup>
0.05 ML Sn, anneal 950 K 3 min	3.0 ± 1.0	5.77 × 10 <sup>12</sup>
0.25 ML Sn	3.3 ± 1.7	8.18 × 10 <sup>12</sup>
0.05 ML Sn at 550 K	3.0 ± 0.9	3.87 × 10 <sup>12</sup>
0.05 ML Sn at 810 K	2.0 ± 0.9	2.84 × 10 <sup>12</sup>
0.25 ML Sn at 810 K	1.4 ± 0.5	1.13 × 10 <sup>13</sup>
0.25 ML Sn at 810 K sputtered	2.3 ± 0.7	7.57 × 10 <sup>12</sup>
0.05 ML Pt	12.7 ± 3.6	2.60 × 10 <sup>11</sup>
0.05 ML Pd	14.9 ± 5.9	1.20 × 10 <sup>11</sup>
0.05 ML Pd, anneal 810 K 3 min	20.0 ± 3.9	8.44 × 10 <sup>10</sup>
0.05 ML Re	9.9 ± 4.4	1.62 × 10 <sup>11</sup>

1–2 layers high, assuming the  $\beta$  tin structure (Figure 1b, Table 1, Figure S1a). Table 1 reports the average cluster heights and cluster densities, while Figures S1–S3 show the cluster height distributions for all of the surfaces in this study. For the 0.02 ML Sn surface, typical cluster diameters range from 30 to 40 Å, but it is likely that the STM tip itself limits the smallest diameter to ~20–30 Å due to tip convolution effects, and therefore the height is expected to be a more accurate measure of cluster size than the diameter.<sup>61,73</sup> There are also two large clusters ~10 Å high and 60–80 Å wide that appear in the 1100 × 1100 Å<sup>2</sup> image. Strong interactions between the STM tip and the Sn clusters result in glitches in the image, and consequently it is more difficult to image Sn on HOPG compared to other metals on HOPG (Ru,<sup>35</sup> Re, and Pd) or Sn on TiO<sub>2</sub>,<sup>45</sup> this behavior is characteristic of tip-cluster interactions that are stronger than the cluster-support interactions. For a higher coverage of 0.05 ML Sn on HOPG (Figure 1c, Figure S1b), the average height of the small clusters is similar ( $3.5 \pm 1.0$  Å), but the cluster density is increased by a factor of 2.9 from  $2.96 \times 10^{12}/\text{cm}^2$  to  $8.60 \times 10^{12}/\text{cm}^2$  (Table 1). Large clusters ~10 Å in height account for <3% of the total number of clusters on the surface for both coverages. When the coverage is increased to 0.25 ML Sn, a greater fraction of the surface is covered by small clusters that range from 35 to 60 Å in diameter and  $3.3 \pm 1.7$  Å in height with a density of  $8.18 \times 10^{12}/\text{cm}^2$  (Figure 1d, Table 1, Figure S1c). There is also a greater number of large clusters that are 55–75 Å in diameter and 7–13 Å high, but these still comprise only ~3% of the total number of clusters. The frequent appearance of glitches in the STM images and partial clusters is again indicative of a strong interaction between the STM tip and the Sn clusters that may result in metal atoms or clusters being picked up or dropped by the STM tip. There are many studies of metal clusters on HOPG in which the clusters were also displaced by STM tip,<sup>11,41</sup> as observed for Pt,<sup>22,74,75</sup> Fe,<sup>1</sup> Cu,<sup>27</sup> and Ru.<sup>21</sup>

STM images of other metals such as Re, Pd, and Pt on HOPG demonstrate that for an identical coverage of 0.05 ML, the cluster sizes are substantially larger than those for Sn/HOPG, and the number of clusters on the surface is correspondingly smaller. For example, for Re clusters on HOPG, the average cluster height is  $9.9 \pm 4.4$  Å, and the number of clusters ( $1.62 \times 10^{11}/\text{cm}^2$ ) is lower by a factor of 50 (Figure 2a, Table 1, Figure S1d). In the case of 0.05 ML Pt on HOPG, the average cluster height is  $12.6 \pm 3.6$  Å with a cluster

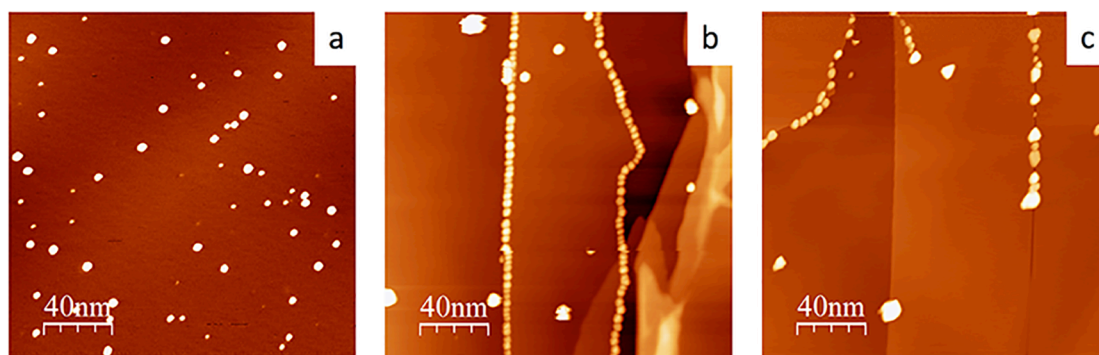


**Figure 2.** STM images for 0.05 ML of the following metals deposited at room temperature on HOPG: (a) Re; (b) Pt; and (c) Pd.

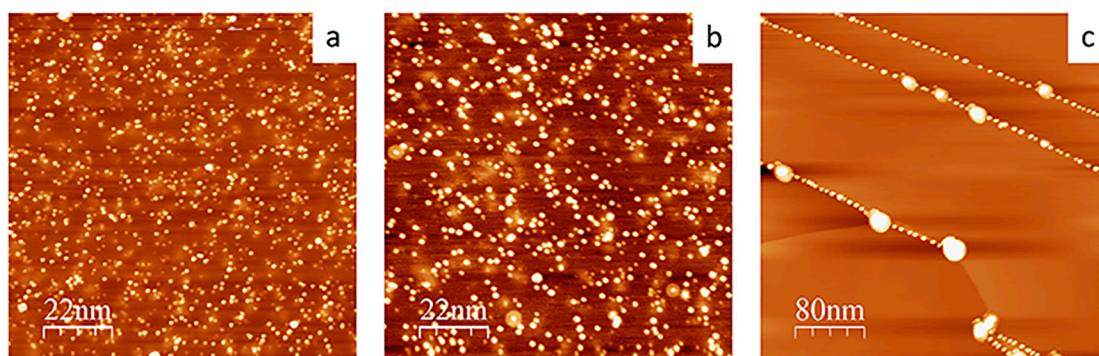


**Figure 3.** STM images for 0.05 ML of the following metals deposited at room temperature on HOPG: (a) Sn annealed to 800 K for 3 min; (b) Sn annealed to 950 K for 3 min; and (c) Pd annealed to 810 K for 3 min.

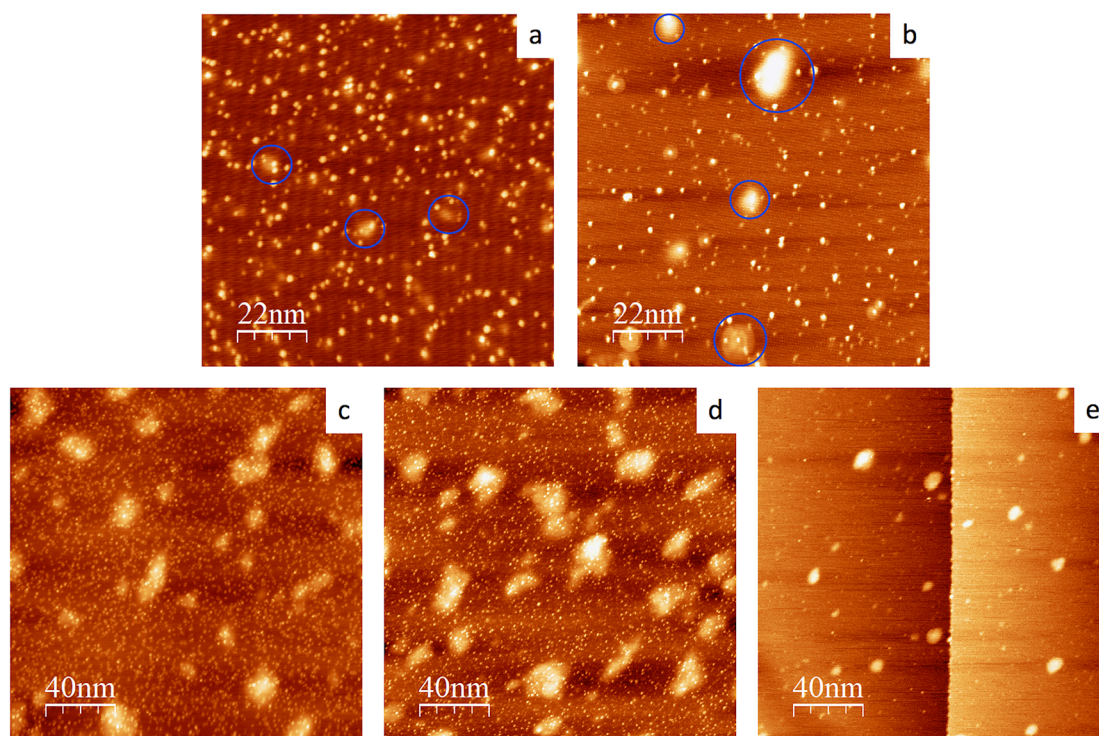


**Figure 4.** STM images for 0.05 ML on Sn on HOPG deposited at (a) 550 K and (b) 810 K; and STM images of 0.25 ML on Sn on HOPG deposited at 810 K on (c) unspattered HOPG and (d) HOPG sputtered with Ar<sup>+</sup> for 10 s at 100  $\mu$ A current to the sample. (e) shows the sputtered HOPG surface in (d) before Sn deposition. The blue circles mark the bubble-like protrusions that appear to be related to subsurface Sn.

density of  $2.60 \times 10^{11}/\text{cm}^2$  (Figure 2b, Table 1, Figure S1e). Moreover, there is a clear preference for the Pt clusters to aggregate at the step edges, which are the preferred low

coordination sites, indicating that diffusion of Pt atoms on the HOPG surface is facile. Re clusters also nucleate at the step edges, but there are many Re clusters that exist on the terraces

as well. Although some large islands are observed on the terraces for Pt on HOPG, these often are associated with an STM tip glitch, which again suggests that the large terrace clusters could be influenced by the interaction with the STM tip.

For 0.05 ML Pd on HOPG, the average cluster height is  $14.9 \pm 5.9$  Å, and the cluster density is  $1.20 \times 10^{11}/\text{cm}^2$  (Figure 2c, Table 1, Figure S1f). Pd clusters also have a tendency to aggregate at line defects, such as step edges, and form large clusters that are generally not observed on the terraces. The Pd clusters exhibit regular shapes such as truncated triangles, implying that diffusion of atoms within the clusters readily occurs to produce thermodynamically favored shapes. Furthermore, Pd and Re clusters are relatively easy to image, unlike the Pt and Sn clusters that strongly interact with the STM tip.

When 0.05 ML of Sn is annealed for 3 min at 800 and 950 K and imaged by STM at room temperature, sintering into larger clusters is surprisingly not observed (Figure 3a,b). For both annealed surfaces, the average cluster heights ( $2.8 \pm 1.1$  and  $3.0 \pm 1.0$  Å, respectively) are slightly smaller than that of the unannealed surface (Table 1, Figure S2a,b). Furthermore, the minor increase in cluster density (8%, Table 1) after annealing to 800 K could be explained by the dissociation of some of the largest clusters into smaller islands. The cluster density decreases to  $\sim 65\%$  of the value on the unannealed surface after annealing to 950 K (Table 1). In this case, the loss of Sn clusters is attributed to Sn sublimation, which is significant at 950 K, based on temperature programmed desorption experiments for Sn on HOPG (Figure S3). These experiments show that the onset of Sn desorption occurs around 800 K, and substantial desorption occurs above 900 K. The 800 and 950 K annealing temperatures were chosen to ensure sufficient energy for atom diffusion and metal–metal bond breaking, which are the two processes involved in cluster sintering, while allowing some fraction of Sn to remain on the surface. In contrast, the annealing of 0.05 ML Pd at 810 K for 3 min results in clusters that are significantly larger than the  $20.0 \pm 3.9$  Å high unannealed clusters. Specifically, on the annealed surface, Pd clusters 30–50 Å in height are observed at the step edges, along with smaller clusters that are 15–20 Å high (Figure 3c). After annealing, the larger Pd clusters grow at the expense of the smaller ones and the total number of clusters on the surface decreases (Table 1).

Sn was also deposited at elevated temperatures in order to determine if Sn–Sn bond breaking rather than Sn atom diffusion on the surface is the rate-limiting step in cluster sintering; if metal–metal bond breaking is the rate-limiting step, then deposition at elevated temperatures would result in larger clusters. For 0.05 ML deposition at 550 K, the average height size remains small ( $3.0 \pm 0.9$  Å), while the cluster density is only 45% of the value for the room temperature surface (Figure 4a, S4a). Based on the lower cluster density and similar average height, it appears that Sn has a lower sticking probability on HOPG at 550 K compared with room temperature. For 0.05 ML deposition at 810 K, STM images show only small clusters on the surface ( $2.0 \pm 0.9$  Å average height, 20–40 Å diameter) with a low cluster density (Figure 4b, Table 1, Figure S4b).

However, larger, bubble-like protrusions that are  $\sim 3.4$  Å high and 200–450 Å wide are observed and marked with blue circles in Figure 4b. STM images of the annealed 0.05 ML Sn clusters (Figure 3a,b) also show evidence of smaller bubble-like

protrusions, and a few of these same features are detected in the unannealed 0.05 ML Sn clusters (Figure 1c, blue circles). Both surfaces prepared by high temperature deposition do not contain larger Sn clusters and are easy to image by STM due to the absence of cluster–tip interactions that are typically observed for Sn on HOPG. For a higher coverage of 0.25 ML Sn deposited at 810 K, the density of the large bubble-like protrusions increases as well as the density of the small 2 Å high clusters (Figure 4c, Table 1, Figure S4c), and in some cases, the  $\sim 2$  Å clusters appear to exist on top of the bubble-like protrusions. Notably, these clusters are smaller and more uniform in size than the ones observed for the lower coverages of 0.02 and 0.05 ML of Sn deposited at room temperature; the larger clusters greater than 4 Å in height observed for 0.25 ML of Sn deposited at room temperature (Figure 1d) are also completely absent at elevated temperature.

The freshly cleaved HOPG surface was lightly sputtered with Ar<sup>+</sup> ions (0.5 keV, 10 s, 100 nA current to the crystal) to introduce defects that can act as portals into the subsurface region. STM images of the resulting surface exhibit protrusions that are 2.0–3.9 Å high and 80–130 Å wide (Figure 4d). The low ion flux and short sputtering time were used so that the surface would not be substantially damaged. These bubble-like features are attributed to subsurface argon and are similar to the ones observed on the surface after high temperature Sn deposition. Thus, the surface for Sn deposited at 810 K exhibits the same type of features associated with subsurface species and might be assigned to subsurface Sn. To test this hypothesis, 0.25 ML Sn was deposited at 810 K on the HOPG surface that was sputtered using the same conditions as in Figure 4d; the introduction of defects into the HOPG substrate is expected to promote diffusion of Sn subsurface and the formation of the bubble-like protrusions. The STM image shown in Figure 4e demonstrates that this surface looks similar to Sn deposited at 810 K on unsputtered HOPG, but a greater fraction of the total surface area is covered by the bubble-like protrusions in the case of the sputtered surface (20% vs 12%); furthermore, the density of the small clusters is 30% lower than on the unsputtered HOPG, and the average height of these clusters is greater ( $2.3 \pm 0.7$  Å, Table 1, Figure S4d). This result is consistent with a greater fraction of deposited Sn diffusing subsurface on the sputtered HOPG, which has more defects that can potentially serve as entry points into the subsurface region. Three dimensional STM images are shown in Figure S5 to better illustrate the bubble-like features on the Sn/HOPG surfaces.

**X-ray Photoelectron Spectroscopy Studies.** For 0.25 ML Sn on HOPG deposited at room temperature (Figure 5), the Sn(3d<sub>5/2</sub>) binding energy of 484.7 eV and peak shape corresponds to metallic Sn.<sup>74</sup> Therefore, there is no evidence of strong interactions between Sn and the HOPG support, which is the expected behavior since Sn is not known to form carbides.<sup>75–77</sup> XPS studies of 0.25 ML of Sn deposited at 810 K show that the Sn signal is barely detectable and 23 times lower in intensity than for 0.25 ML of Sn deposited at room temperature (Figure 5). Based on the integrated Sn(3d<sub>5/2</sub>) signals for 0.005 ML and 0.25 ML Sn deposited at 810 K (Figure 5), the actual Sn coverage on latter surface was estimated to be  $\sim 0.007$  ML. This in contrast to the much higher coverage of 0.25 ML determined from the flux from the Sn source and the deposition time; thus, it appears that the sticking coefficient of Sn on HOPG is significantly lower than unity at 810 K, as also observed for other metals deposited on

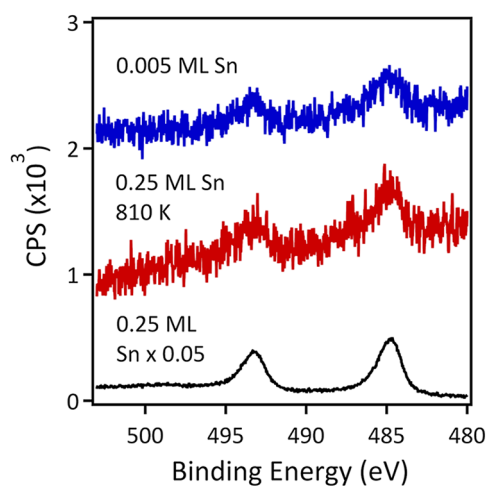


**Figure 5.** XPS data for the Sn(3d) region for 0.25 ML of Sn deposited at room temperature (black); 0.25 ML of Sn deposited at 810 K (red); and 0.005 ML of Sn deposited at room temperature (blue).

HOPG at high temperature<sup>11</sup> such as Pt,<sup>22</sup> Ag,<sup>26</sup> and Fe.<sup>41</sup> Similarly, the sticking coefficients must be close to zero for Re and Pd deposition at 810 K because almost no metal clusters are detected in the STM images of these surfaces. The Sn(3d<sub>5/2</sub>) peak for the high temperature deposition is slightly broader than for 0.005 ML at room temperature, which may suggest the presence of Sn species with a different environment from metallic Sn on the surface of HOPG. Assuming that the small clusters observed in the STM image for 0.25 ML deposited at 810 K (Figure 5) correspond to single Sn atoms on the surface of HOPG, the estimated coverage would be 0.0075 ML based on the number of clusters on the surface. This value is in general agreement with the experimentally observed ~0.007 ML coverage determined from the Sn(3d<sub>5/2</sub>) XPS intensities, but it is also still consistent with Sn covered by a single HOPG layer, which would attenuate the Sn signal by only 14% (see Supporting Information). If the Sn clusters were larger than a single atom, they would need to be covered by more than one layer of HOPG; for example, the Sn clusters would need to be covered by 4 layers of graphene in order for the experimental Sn(3d<sub>5/2</sub>) intensity to be consistent with Sn<sub>2</sub> clusters (see Supporting Information).

For the surface consisting of 0.25 ML of Sn deposited at 810 K, Sn is oxidized after exposure to  $5 \times 10^{-6}$  Torr of O<sub>2</sub> at room temperature for 5 min under directed dosing conditions, in which the local pressure is estimated to be 10 times higher than the chamber pressure (Figure S6).<sup>54</sup> A shift in the Sn(3d<sub>5/2</sub>) to higher binding energy is detected after oxidation, and the extent of this shift is similar to what is observed for 0.25 ML of Sn clusters deposited at room temperature after oxidation under identical conditions (Figure S6). The observed oxidation of Sn implies that for Sn deposited at 810 K, there is still some fraction of Sn clusters on top of HOPG rather than in the subsurface.

**DFT Studies.** DFT studies were carried out to understand why the Sn clusters on HOPG are significantly smaller than those for metals like Pd, Pt, and Re. Both kinetic and thermodynamic driving forces are considered to explain the small Sn clusters. In terms of kinetics, small clusters could result from the rate of deposition being faster than the rate of diffusion. However, calculations of metal atom diffusion on HOPG yield activation energy barriers of 0.04, 0.22, 0.61, and

0.06 eV for Pt, Pd, Re, and Sn, respectively. The fact that Sn has a diffusion barrier that is lower than or comparable to those of the other metals demonstrates that the small size of the Sn clusters is not due to kinetic limitations for atom diffusion.

A second possibility is that the small Sn cluster size is dictated by thermodynamic factors. Figure 6 shows the binding

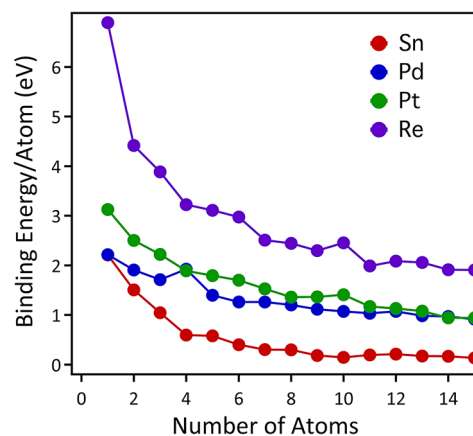


**Figure 6.** Binding energies per atom for Sn, Pd, Pt, and Re on pristine HOPG.

energies per atom for Sn, Pd, Pt, and Re as a function of increasing cluster size from 1 to 15 atoms, with the reference energy taken as the energy of the atom in the bulk. Examples of the structures of the Sn and Re clusters are provided in Figure S7. In all cases, the binding energies are large positive values and decrease with increasing cluster size. For example, the binding energy of a single atom of Sn on HOPG is 2.2 eV, which is consistent with weak interactions between Sn and HOPG compared to Sn–Sn interactions in the bulk. For all of the metals, the binding energies/atom achieve close to their minimum values at a cluster size of ~10 atoms; this is presumably due to the fact that the metal–metal bonds are more difficult to break when the atoms are not fully coordinated in the smaller clusters. The behavior of Sn is unique in that the binding energies/atom for Sn<sub>10</sub>–Sn<sub>15</sub> clusters are only ~0.2 eV higher than those of Sn in the bulk. Thus, for the Sn atoms on HOPG, there is little thermodynamic driving force for the cluster size to increase beyond ~10 atoms. In contrast, the atoms in the largest Pt and Pd clusters are more than 1 eV higher in energy than in the bulk, while Re atoms are more than 2 eV higher in energy. Similar trends are observed for these metals on HOPG with a carbon vacancy defect or a Stone–Wales defect, as well as for the metal clusters in a vacuum (Figure S8). Specifically, the per atom energies for Sn<sub>n</sub> ( $n \geq 10$ ) are only slightly greater (~0.25 eV) than those for Sn in the bulk, while these values are 0.6 eV or higher for 10–15 atom clusters of the other metals studied. It should be noted that the single atoms at the carbon vacancy defects have negative binding energies due to the strong interactions with the undercoordinated carbon atoms in the surface.

DFT calculations were also conducted to address whether it is energetically favorable for Sn to reside in the subsurface. As shown in Figure S9a, the binding energies for a single atom in the subsurface are >1.8 eV for the four metals studied here, and although the per atom binding energies decrease with increasing cluster size, the value for Sn<sub>9</sub> is still almost 1 eV.

Calculations for subsurface Sn atoms in the presence of a surface vacancy also demonstrate that Sn clusters of 1–9 atoms are not energetically favorable, and the same is true for Pd, Pt, and Re clusters larger than 2 atoms (Figure S9b). However, the binding energy of a subsurface Sn atom at a subsurface vacancy (−1.8 eV) is lower than the binding energy of a Sn atom in the bulk (Figure 7, structures shown in Figure S10).

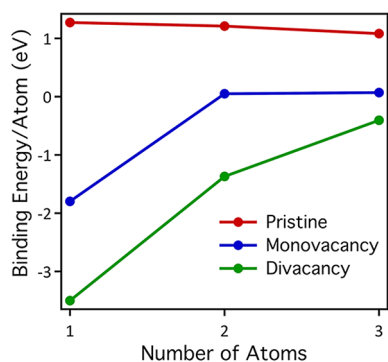


**Figure 7.** Binding energies/atom for subsurface Sn on pristine HOPG (red), at a monovacancy (blue), and at a divacancy (green).

For Sn<sub>2</sub> and Sn<sub>3</sub> clusters at subsurface vacancies, the per atom binding energies are approximately the same as for the clusters at the pristine HOPG surface, suggesting that there is no strong thermodynamic driving force for these larger Sn clusters to exist subsurface. At a subsurface divacancy, the energy of the Sn atom is 3.5 eV lower than that of Sn in the bulk and 1.7 eV lower than that of Sn at a subsurface monovacancy (Figure 7). When the number of Sn atoms in the cluster is increased to 2 and 3, the energies remain lower than for Sn atoms in the bulk by 1.4 and 0.4 eV, respectively. In contrast, Sn clusters of 1–3 atoms in the subsurface in the absence of a vacancy have binding energies that are more than 1 eV higher than those of Sn clusters in the bulk (Figure 7). Furthermore, for a Sn<sub>3</sub>

cluster at a subsurface monovacancy site, the creation of a divacancy via the removal of a carbon atom results in an energy change of −1.07 eV. Thus, the growth of this subsurface vacancy site is promoted in the presence of Sn.

**Simulated STM Images.** Simulated STM images were generated from the DFT isosurfaces in order to gain further insight into the nature of the Sn clusters on HOPG. Figure 8 shows simulated STM images of Sn clusters with sizes of 1, 4, and 10 atoms on the surface and in the subsurface, as well as Sn<sub>4</sub> at a subsurface monovacancy; atomic structures for these surfaces are shown in Figures S11 and S12. For all sizes, a Sn cluster on the surface appears larger than the same size cluster in the subsurface, and diameters of the clusters are larger for the subsurface clusters. The Sn<sub>4</sub> subsurface cluster at a subsurface monovacancy is also lower than the Sn<sub>4</sub> cluster at the surface or in the subsurface. The appearance of the simulated STM images Sn<sub>1</sub>–Sn<sub>10</sub> clusters are generally consistent with the experimental images containing clusters of the same sizes (Figure 1a), although it is not possible to definitively distinguish surface from subsurface clusters based on the simulated images. The line profiles of these clusters (Figure S13) demonstrate that the Sn<sub>1</sub> and Sn<sub>4</sub> surface clusters have heights larger than those of their subsurface counterparts, and the Sn<sub>4</sub> subsurface cluster at a subsurface vacancy has the lowest height of any of the Sn<sub>4</sub> clusters. The simulated height for the surface Sn<sub>1</sub> species is 3.0 Å, which is in good agreement with the empirical diameter of the Sn atom (2.9 Å),<sup>78</sup> whereas the simulated height of subsurface Sn<sub>1</sub> is 1.9 Å. The most stable Sn<sub>4</sub> cluster on the surface is two atoms high and has a simulated height of 4.5 Å, while the single-layer subsurface Sn<sub>4</sub> cluster has a simulated height of 2.9 Å, and subsurface Sn<sub>4</sub> at a subsurface vacancy has an even smaller height of 1.4 Å. Experimental STM cluster profiles are shown in Figure S14 for a comparison with the simulated data.

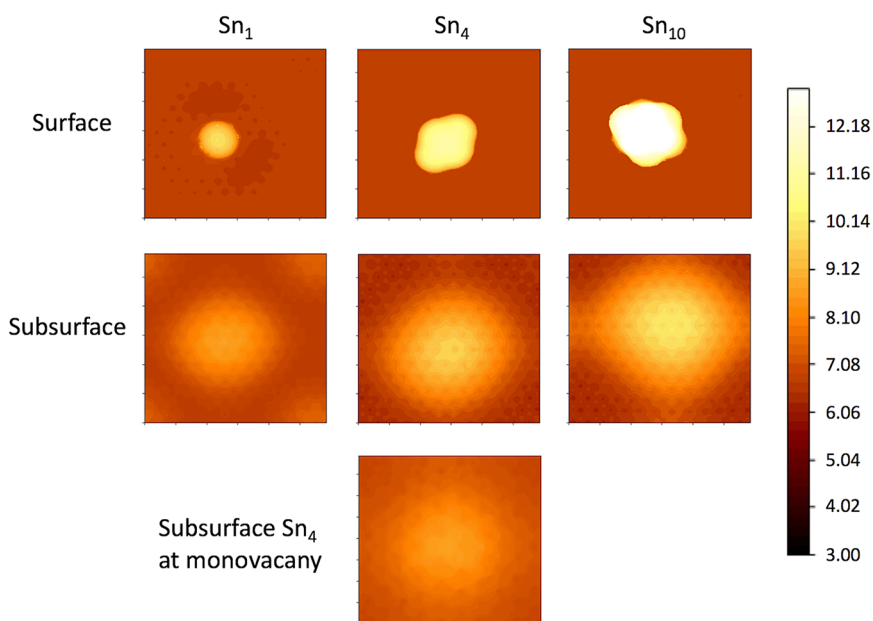


**Figure 8.** Simulated STM images for Sn<sub>1</sub>, Sn<sub>4</sub>, and Sn<sub>10</sub> clusters on the HOPG surface and in the subsurface, and a Sn<sub>4</sub> cluster in the subsurface at a subsurface monovacancy. The top 6 images are 29.1 Å × 29.4 Å, and the bottom image is 20.0 Å × 21.5 Å. The vertical scale bar is in units of Å.

## DISCUSSION

The deposition of 0.05 ML Sn on pristine HOPG results in small clusters ( $2.4 \pm 1.4$  Å high), whereas Pt, Pd, and Re deposited under the same conditions exhibit much larger cluster sizes (9–13 Å high). Furthermore, the size of the Sn cluster remains small after annealing to 800 and 950 K, in contrast to the large Pd clusters observed after annealing to 810 K. The existence of only small Sn clusters on pristine HOPG under any deposition and annealing conditions is unique with respect to the behavior of transition metals<sup>11,13,20–22,27,31,37</sup> and the post-transition metals (Ge,<sup>14,15</sup> and Sb<sup>15–17</sup>) that are neighbors of Sn in the periodic table. In general, it is expected that metal and semimetal atoms on HOPG should be mobile, given that the adatom interactions with HOPG are primarily through weak van der Waals forces.<sup>11,41</sup>

The unusual behavior of Sn on HOPG can be attributed to the weak metal–metal interactions compared to that of the transition metals, and this behavior is consistent with the relatively low heat of sublimation for Sn (70 kcal/mol)<sup>79</sup> vs transition metals such as Pt (135 kcal/mol),<sup>80</sup> Pd (89 kcal/mol),<sup>81</sup> and Re (186 kcal/mol).<sup>82</sup> Consequently, there is no strong thermodynamic driving force for the Sn atoms to aggregate into larger, bulk-like clusters because the stability of a Sn atom in the bulk is not much higher than a Sn atom in a 10-atom cluster on HOPG (0.2 eV, Figure 6). In contrast, Pd, Pt, and Re atoms are 1–2 eV more stable in the bulk than in 10-atom surface clusters. Since the diffusion barrier for a Sn atom on HOPG (0.06 eV) is lower than or comparable to that of Pt, Pd, and Re atoms (0.04–0.6 eV), which form large clusters on HOPG, the small sizes of the Sn clusters on HOPG are attributed to thermodynamic rather than kinetic factors. The growth of small Sn clusters is also consistent with the relative surface free energies ( $\gamma$ ) of Sn and HOPG. Two dimensional (2D) metal cluster formation is thermodynamically favored when  $\gamma_{\text{support}}$  is large;  $\gamma_{\text{metal}}$  is small; and the metal–substrate interaction is strong.<sup>83</sup> In the case of Sn on HOPG, only the low  $\gamma_{\text{Sn}}$  ( $0.5 \text{ J/m}^2$ )<sup>84</sup> favors 2D growth, whereas the weak Sn–HOPG interactions and  $\gamma_{\text{HOPG}}$  ( $0.14\text{--}0.15 \text{ J/m}^2$ )<sup>85</sup> do not. Although  $\gamma_{\text{Sn}}$  is larger than  $\gamma_{\text{HOPG}}$ , entropy favors the formation of small 2D Sn clusters over aggregation into large 3D clusters at low coverages. Notably, low values for  $\gamma_{\text{metal}}$ , favoring 2D growth, also correspond to weak metal–metal bonds and low sublimation energies.

There is strong evidence that subsurface Sn formation is induced by high temperature deposition or annealing. Bubble-like features  $\sim 1.5\text{--}3$  Å height and ranging from 200 to 450 Å in diameter are observed for Sn deposition at 810 K (Figures 4c and S5) and attributed to subsurface Sn species. The Sn-induced bubble-like features are similar to those observed for subsurface Ar on HOPG. These same features are detected after sputtering HOPG and disappear after the surface is heated to induce Ar desorption. Furthermore, the presence of clusters smaller than 2 Å in height suggests that the small clusters could be from subsurface atoms, given that the sub-2 Å high clusters are smaller than the 2.9 Å diameter of a Sn atom. Simulated STM images indicate that subsurface Sn atoms and subsurface Sn<sub>4</sub> clusters at a subsurface vacancy should have heights below 2 Å. Nearly all of the bubble-like features have one or more clusters on top of them. These are likely to be Sn surface clusters that are perhaps trapped at a defect; although they are relatively small, their heights are typically larger than 2

Å, and therefore, it is reasonable to assign them to surface clusters. The surface consisting of 0.25 ML Sn deposited at 810 K is oxidized by exposure to  $1 \times 10^{-6}$  Torr O<sub>2</sub> at room temperature, implying that there is some fraction of Sn at the surface that is readily oxidized and not deep in the subsurface.

The fact that the bubble-like features and sub-2 Å clusters attributed to subsurface Sn both increase with increasing deposition and annealing temperatures is consistent with the expected promotion of Sn migration into the subsurface at higher temperatures. For 0.05 ML Sn clusters deposited at room temperature, <1% of the clusters are smaller than 2 Å (Figure S1b), but upon annealing to 800 or 950 K, this fraction increases to 25% (Figure S2a,b). For 0.05 ML Sn clusters deposited at 550 K, the fraction of clusters smaller than 2 Å is 11%, and at the higher deposition temperature of 810 K, this fraction increases to 75–85% (Figure S4a,b). Interestingly, the fraction of sub-2 Å clusters is lower for 0.25 ML Sn deposited at 810 K on the sputtered surface (39%) compared to the unspattered HOPG (86%). One possible explanation is that the Sn atoms are less mobile on the sputtered surface because they are trapped at vacancy defect sites, and consequently, the surface atoms are less likely to migrate to the steps and enter the subsurface.

Studies by the Thiel and Evans group report subsurface metal clusters on HOPG for Cu, Fe, Ru, Pt, and Dy.<sup>41</sup> In all of these cases, the HOPG surface was first bombarded with Ar<sup>+</sup> ions to introduce vacancy defects that provide portals through which the metal atoms can enter the subsurface. Deposition was carried out at elevated temperature so that the metal atoms would not be trapped at the low-coordination vacancy defects. Large, faceted subsurface metal islands with average heights of 13–35 atomic layers were observed for Cu<sup>27</sup> and Fe,<sup>1</sup> whereas smaller faceted subsurface clusters  $\sim 3$  atomic layers high were observed for Ru<sup>43</sup> and Dy,<sup>42</sup> and Pt<sup>44</sup> exhibited 3-layer rounded subsurface clusters. For the Cu and Fe deposited on HOPG, clusters as small as  $\sim 2$  Å in height were observed on top of the faceted subsurface clusters and on HOPG itself;<sup>1,27</sup> these features were attributed to defects decorated by bare metal atoms and resemble the small Sn clusters observed in this work. For Sn deposition at elevated temperatures, the appearance of subsurface features occurs on a pristine, unspattered HOPG surface. One possibility is that the Sn atoms enter the subsurface via the step edges and then readily diffuse in the subsurface region; this behavior has also been suggested for intercalation of other species into pristine graphite.<sup>38,39</sup> In our experiments, Sn deposition occurred through electron bombardment of a Sn-containing crucible, and it is possible that the metal flux contains high energy ions that could potentially damage the surface. However, it does not appear that high energy Sn ions were involved in the formation of subsurface Sn because the STM images from experiments carried out with a +600–800 V bias on the surface to exclude Sn ions were the same as the images collected without the bias.

Although alkali and alkaline earth metals<sup>38,86</sup> are known to readily intercalate into pristine graphite, Sn intercalation is not expected based on DFT calculations. It is not energetically favorable for Sn atoms to exist under a single layer of HOPG due to the high energy cost of separating the HOPG layers compared to the weak Sn–HOPG interactions, whereas alkali metals have stronger admetal–graphite interactions that favor intercalation.<sup>11</sup> However, DFT calculations also demonstrate that a subsurface Sn atom at a subsurface vacancy is lower in energy than a Sn atom at the surface, thus providing a scenario

in which Sn can exist subsurface. Moreover, subsurface Sn<sub>n</sub> clusters ( $n = 1-3$ ) at a subsurface divacancy are more stable than the clusters at the surface. Calculations also suggest that the presence of subsurface Sn could induce existing subsurface vacancies to grow in size. Specifically, the energy of a Sn atom at a subsurface vacancy decreases when another vacancy is added to form Sn at a subsurface divacancy.

## CONCLUSIONS

Small Sn clusters are observed on the noninteracting HOPG surface, implying that Sn is likely to form a uniform layer that completely covers the surface. Since this behavior is attributed to the lack of thermodynamic driving force to form Sn–Sn bonds in large clusters and is not associated with Sn–substrate interactions, it is reasonable to expect that Sn should form uniform layers on any substrate surface. Furthermore, there is evidence that Sn migrates subsurface at elevated temperatures, which would promote the stability of Sn–graphite composites used in alkali-ion batteries and other applications. For applications in Li ion batteries, the small particle sizes for Sn on graphite are desirable for improving stability during cycling by minimizing the absolute volume change during lithiation.<sup>2,7–10</sup>

## ASSOCIATED CONTENT

### Supporting Information

The Supporting Information is available free of charge at <https://pubs.acs.org/doi/10.1021/acs.jpcc.3c08215>.

Cluster height histograms for Sn, Re, Pd, and Pt clusters on HOPG after room temperature deposition, Sn and Pt clusters on HOPG after annealing, and Sn clusters deposited on HOPG at elevated temperatures; TPD data for Sn desorption from HOPG; 3D STM images of Sn deposited on HOPG at elevated temperatures and annealed after deposition at room temperature; XPS data for Sn on HOPG before and after exposure to O<sub>2</sub>; Atomic structures of Sn and Re clusters on HOPG used for DFT calculations; Binding energies for Sn, Pd, Pt, and Re in vacuum and on HOPG at defects; Binding energies for Sn, Pd, Pt, and Re in the subsurface of pristine HOPG and HOPG with a surface vacancy; Atomic structures for subsurface Sn clusters on HOPG with and without vacancies; Atomic structures used in the STM simulations for Sn on pristine HOPG; Atomic structures used in the STM simulations for subsurface Sn clusters; Simulated and experimental STM line profiles; Calculation of Sn XPS signal for Sn clusters covered by HOPG (PDF)

## AUTHOR INFORMATION

### Corresponding Author

Donna A. Chen – Department of Chemistry and Biochemistry, University of South Carolina, Columbia, South Carolina 29208, United States; [orcid.org/0000-0003-4962-5530](https://orcid.org/0000-0003-4962-5530); Phone: 803-777-1050; Email: [dachen@sc.edu](mailto:dachen@sc.edu); Fax: 803-777-9521

### Authors

Sumit Beniwal – Department of Chemistry and Biochemistry, University of South Carolina, Columbia, South Carolina 29208, United States; [orcid.org/0000-0002-9381-5481](https://orcid.org/0000-0002-9381-5481)

Wenrui Chai – Department of Chemistry, University of Texas, Austin, Texas 78712, United States; [orcid.org/0000-0002-5801-0135](https://orcid.org/0000-0002-5801-0135)

Mengxiong Qiao – Department of Chemistry and Biochemistry, University of South Carolina, Columbia, South Carolina 29208, United States

Zahra Bajalan – Department of Chemistry, University of Texas, Austin, Texas 78712, United States

Ali S. Ahsen – Department of Chemistry and Biochemistry, University of South Carolina, Columbia, South Carolina 29208, United States

Kasala P. Reddy – Department of Chemistry and Biochemistry, University of South Carolina, Columbia, South Carolina 29208, United States

Yankun Chen – Department of Chemistry, University of Texas, Austin, Texas 78712, United States

Graeme Henkelman – Department of Chemistry, University of Texas, Austin, Texas 78712, United States; [orcid.org/0000-0002-0336-7153](https://orcid.org/0000-0002-0336-7153)

Complete contact information is available at: <https://pubs.acs.org/doi/10.1021/acs.jpcc.3c08215>

## Notes

The authors declare no competing financial interest.

## ACKNOWLEDGMENTS

We gratefully acknowledge financial support from the National Science Foundation (CHE 1764164). G.H. also acknowledges the Welch Foundation (F-1841) and computational resources at the Texas Advanced Computing Center. W.C. and Y.C. thank the Freshman Research Initiative program at the University of Texas at Austin for support.

## REFERENCES

- (1) Lii-Rosales, A.; Han, Y.; Lai, K. C.; Jing, D. P.; Tringides, M. C.; Evans, J. W.; Thiel, P. A. Fabricating Fe Nanocrystals Via Encapsulation at the Graphite Surface. *J. Vac. Sci. Technol. A* **2019**, *37*, No. 061403.
- (2) Wang, J.; Kober, D.; Shao, G. F.; Epping, J. D.; Gorke, O.; Li, S.; Gurlo, A.; Bekheet, M. F. Stable Anodes for Lithium-Ion Batteries Based on Tin-Containing Silicon Oxycarbonitride Ceramic Nanocomposites. *Mater. Today Energy* **2022**, *26*, No. 100989.
- (3) Inomata, Y.; Albrecht, K.; Yamamoto, K. Size-Dependent Oxidation State and CO Oxidation Activity of Tin Oxide Clusters. *ACS Catal.* **2018**, *8*, 451–456.
- (4) Deng, L. D.; Miura, H.; Shishido, T.; Wang, Z.; Hosokawa, S.; Teramura, K.; Tanaka, T. Elucidating Strong Metal-Support Interactions in Pt-Sn/SiO<sub>2</sub> Catalyst and Its Consequences for Dehydrogenation of Lower Alkanes. *J. Catal.* **2018**, *365*, 277–291.
- (5) Srisakwattana, T.; Suriye, K.; Prasertdam, P.; Panpranot, J. Preparation of Aluminum Magnesium Oxide by Different Methods for Use as PtSn Catalyst Supports in Propane Dehydrogenation. *Catal. Today* **2020**, *358*, 90–99.
- (6) Michalak, W. D.; Krier, J. M.; Alayoglu, S.; Shin, J. Y.; An, K.; Komvopoulos, K.; Liu, Z.; Somorjai, G. A. CO Oxidation on PtSn Nanoparticle Catalysts Occurs at the Interface of Pt and Sn Oxide Domains Formed under Reaction Conditions. *J. Catal.* **2014**, *312*, 17–25.
- (7) Zeb, G.; Gaskell, P.; Le, X. T.; Xiao, X. C.; Szkopek, T.; Cerruti, M. Decoration of Graphitic Surfaces with Sn Nanoparticles through Surface Functionalization Using Diazonium Chemistry. *Langmuir* **2012**, *28*, 13042–13050.
- (8) Palaniselvam, T.; Freytag, A. I.; Moon, H.; Janssen, K. A.; Passerini, S.; Adelhalm, P. Tin-Graphite Composite as a High-

- Capacity Anode for All-Solid-State Li-Ion Batteries. *J. Phys. Chem. C* **2022**, *126*, 13043–13052.
- (9) Palaniselvam, T.; Goktas, M.; Anothumakkool, B.; Sun, Y. N.; Schmuch, R.; Zhao, L.; Han, B. H.; Winter, M.; Adelhelm, P. Sodium Storage and Electrode Dynamics of Tin-Carbon Composite Electrodes from Bulk Precursors for Sodium-Ion Batteries. *Adv. Funct. Mater.* **2019**, *29*, No. 1900790.
- (10) Maresca, G.; Tsurumaki, A.; Suzuki, N.; Yoshida, K.; Panero, S.; Aihara, Y.; Navarra, M. A. Sn/C Composite Anodes for Bulk-Type All-Solid-State Batteries. *Electrochim. Acta* **2021**, *395*, No. 139104.
- (11) Appy, D.; Lei, H. P.; Wang, C. Z.; Tringides, M. C.; Liu, D. J.; Evans, J. W.; Thiel, P. A. Transition Metals on the (0001) Surface of Graphite: Fundamental Aspects of Adsorption, Diffusion, and Morphology. *Prog. Surf. Sci.* **2014**, *89*, 219–238.
- (12) Gao, J. Z.; Guo, Q. M. Pinning Platinum and Pt-Oxide Nanoparticles on Graphite. *Appl. Surf. Sci.* **2012**, *258*, 5412–5417.
- (13) Zhang, H.; Fu, Q.; Yao, Y. X.; Zhang, Z.; Ma, T.; Tan, D. L.; Bao, X. H. Size-Dependent Surface Reactions of Ag Nanoparticles Supported on Highly Oriented Pyrolytic Graphite. *Langmuir* **2008**, *24*, 10874–10878.
- (14) Kushvaha, S. S.; Yan, Z. J.; Xu, M. J.; Xiao, W. D.; Wang, X. S. In Situ STM Investigation of Ge Nanostructures with and without Sb on Graphite. *Surf. Rev. Lett.* **2006**, *13*, 241–249.
- (15) Xiao, W. D.; Yan, Z. J.; Kushvaha, S. S.; Xu, M. J.; Wang, X. S. Different Growth Behavior of Ge, Al and Sb on Graphite. *Surf. Rev. Lett.* **2006**, *13*, 287–296.
- (16) Wang, X. S.; Kushvaha, S. S.; Yan, Z.; Xiao, W. Self-Assembly of Antimony Nanowires on Graphite. *Appl. Phys. Lett.* **2006**, *88*, No. 233105.
- (17) Kushvaha, S. S.; Yan, Z.; Xiao, W.; Wang, X. S. Surface Morphology of Crystalline Antimony Islands on Graphite at Room Temperature. *J. Phys. Condes. Matter* **2006**, *18*, 3425–3434.
- (18) Kushvaha, S. S.; Zhang, H. L.; Yan, Z.; Wee, A. T. S.; Wang, X. S. Growth of Self-Assembled Mn, Sb and MnSb Nanostructures on Highly Oriented Pyrolytic Graphite. *Thin Solid Films* **2012**, *520*, 6909–6915.
- (19) Shimonaka, M.; Nakamura, Y.; Kikkawa, J.; Sakai, A. Self-Assembly of Ge Clusters on Highly Oriented Pyrolytic Graphite Surfaces. *Surf. Sci.* **2014**, *628*, 82–85.
- (20) Marz, M.; Sagisaka, K.; Fujita, D. Ni Nanocrystals on HOPG(0001): A Scanning Tunneling Microscope Study. *Beilstein J. Nanotechnol.* **2013**, *4*, 406–417.
- (21) Nielsen, R. M.; Murphy, S.; Strebel, C.; Johansson, M.; Nielsen, J. H.; Chorkendorff, I. A Comparative STM Study of Ru Nanoparticles Deposited on HOPG by Mass-Selected Gas Aggregation Versus Thermal Evaporation. *Surf. Sci.* **2009**, *603*, 3420–3430.
- (22) Howells, A. R.; Hung, L.; Chottiner, G. S.; Scherson, D. A. Effects of Substrate Defect Density and Annealing Temperature on the Nature of Pt Clusters Vapor Deposited on the Basal Plane of Highly Oriented Pyrolytic Graphite. *Solid State Ion.* **2002**, *150*, 53–62.
- (23) Howells, A.; Harris, T.; Sashikata, K.; Chottiner, G. S.; Scherson, D. A. Model Systems in Electrocatalysis: Electronic and Structural Characterization of Vapor Deposited Platinum on the Basal Plane of Highly Oriented Pyrolytic Graphite. *Solid State Ion.* **1997**, *94*, 115–121.
- (24) Kalinkin, A. V.; Sorokin, A. M.; Smirnov, M. Y.; Bukhtiyarov, V. I. Size Effect in the Oxidation of Platinum Nanoparticles on Graphite with Nitrogen Dioxide: An XPS and STM Study. *Kinet. Catal.* **2014**, *55*, 354–360.
- (25) Smirnov, M. Y.; Kalinkin, A. V.; Sorokin, A. M.; Bukhtiyarov, V. I. Room Temperature Interaction of NO<sub>2</sub> with Palladium Nanoparticles Supported on a Nonactivated Surface of Highly Oriented Pyrolytic Graphite (HOPG). *Kinet. Catal.* **2020**, *61*, 907–911.
- (26) Lopez-Salido, I.; Lim, D. C.; Kim, Y. D. Ag Nanoparticles on Highly Ordered Pyrolytic Graphite (HOPG) Surfaces Studied Using STM and XPS. *Surf. Sci.* **2005**, *588*, 6–18.
- (27) Lii-Rosales, A.; Han, Y.; Evans, J. W.; Jing, D. P.; Zhou, Y. H.; Tringides, M. C.; Kim, M. S.; Wang, C. Z.; Thiel, P. A. Formation of Multilayer Cu Islands Embedded beneath the Surface of Graphite: Characterization and Fundamental Insights. *J. Phys. Chem. C* **2018**, *122*, 4454–4469.
- (28) Appy, D.; Lei, H. P.; Han, Y.; Wang, C. Z.; Tringides, M. C.; Shao, D. H.; Kwolek, E. J.; Evans, J. W.; Thiel, P. A. Determining Whether Metals Nucleate Homogeneously on Graphite: A Case Study with Copper. *Phys. Rev. B* **2014**, *90*, No. 195406.
- (29) Wepasnick, K. A.; Li, X.; Mangler, T.; Noessner, S.; Wolke, C.; Grossmann, M.; Gantefoer, G.; Fairbrother, D. H.; Bowen, K. H. Surface Morphologies of Size-Selected Mo<sub>100±2.5</sub> and (MoO<sub>3</sub>)<sub>67±1.5</sub> Clusters Soft-Landed onto HOPG. *J. Phys. Chem. C* **2011**, *115*, 12299–12307.
- (30) Kettner, M.; Maisel, S.; Stumm, C.; Schwarz, M.; Schuschke, C.; Gorling, A.; Libuda, J. Pd-Ga Model Scalms: Characterization and Stability of Pd Single Atom Sites. *J. Catal.* **2019**, *369*, 33–46.
- (31) Kettner, M.; Stumm, C.; Schwarz, M.; Schuschke, C.; Libuda, J. Pd Model Catalysts on Clean and Modified HOPG: Growth, Adsorption Properties, and Stability. *Surf. Sci.* **2019**, *679*, 64–73.
- (32) Bukhtiyarov, A. V.; Burueva, D. B.; Prosvirin, I. P.; Klyushin, A. Y.; Panafidin, M. A.; Kovtunov, K. V.; Bukhtiyarov, V. I.; Koptuyug, I. V. Bimetallic Pd-Au/Highly Oriented Pyrolytic Graphite Catalysts: From Composition to Pairwise Parahydrogen Addition Selectivity. *J. Phys. Chem. C* **2018**, *122*, 18588–18595.
- (33) Ju, W.; Favaro, M.; Durante, C.; Perini, L.; Agnoli, S.; Schneider, O.; Stimming, U.; Granozzi, G. Pd Nanoparticles Deposited on Nitrogen-Doped HOPG: New Insights into the Pd-Catalyzed Oxygen Reduction Reaction. *Electrochim. Acta* **2014**, *141*, 89–101.
- (34) Favaro, M.; Agnoli, S.; Perini, L.; Durante, C.; Gennaro, A.; Granozzi, G. Palladium Nanoparticles Supported on Nitrogen-Doped HOPG: a Surface Science and Electrochemical Study. *Phys. Chem. Chem. Phys.* **2013**, *15*, 2923–2931.
- (35) Galhenage, R. P.; Xie, K.; Diao, W.; Tengco, J. M. M.; Seuser, G. S.; Monnier, J. R.; Chen, D. A. Platinum-Ruthenium Bimetallic Clusters on Graphite: a Comparison of Vapor Deposition and Electroless Deposition Methods. *Phys. Chem. Chem. Phys.* **2015**, *17*, 28354–28363.
- (36) Hovel, H.; Becker, T.; Bettac, A.; Reihl, B.; Tschudy, M.; Williams, E. J. Controlled Cluster Condensation into Preformed Nanometer-Sized Pits. *J. Appl. Phys.* **1997**, *81*, 154–158.
- (37) Kholmanov, I. N.; Gavioli, L.; Fanetti, M.; Casella, M.; Cepek, C.; Mattevi, C.; Sancrotti, M. Effect of Substrate Surface Defects on the Morphology of Fe Film Deposited on Graphite. *Surf. Sci.* **2007**, *601*, 188–192.
- (38) Buttner, M.; Choudhury, P.; Johnson, J. K.; Yates, J. T. Vacancy Clusters as Entry Ports for Cesium Intercalation in Graphite. *Carbon* **2011**, *49*, 3937–3952.
- (39) Dresselhaus, M. S.; Dresselhaus, G. Intercalation Compounds of Graphite. *Adv. Phys.* **2002**, *51*, 1–186.
- (40) Caragiu, M.; Finberg, S. Alkali Metal Adsorption on Graphite: a Review. *J. Phys. Condes. Matter* **2005**, *17*, R995–R1024.
- (41) Lii-Rosales, A.; Han, Y.; Jing, D. P.; Tringides, M. C.; Julien, S.; Wan, K. T.; Wang, C. Z.; Lai, K. C.; Evans, J. W.; Thiel, P. A. Encapsulation of Metal Nanoparticles at the Surface of a Prototypical Layered Material. *Nanoscale* **2021**, *13*, 1485–1506.
- (42) Zhou, Y. H.; Lii-Rosales, A.; Kim, M.; Wallingford, M.; Jing, D. P.; Tringides, M. C.; Wang, C. Z.; Thiel, P. A. Defect-Mediated, Thermally-Activated Encapsulation of Metals at the Surface of Graphite. *Carbon* **2018**, *127*, 305–311.
- (43) Lii-Rosales, A.; Han, Y.; Yu, K. M.; Jing, D. P.; Anderson, N.; Vaknin, D.; Tringides, M. C.; Evans, J. W.; Altman, M. S.; Thiel, P. A. Reverse-Engineering of Graphene on Metal Surfaces: a Case Study of Embedded Ruthenium. *Nanotechnology* **2018**, *29*, No. S05601.
- (44) Lii-Rosales, A.; Han, Y.; Jing, D. P.; Tringides, M. C.; Thiel, P. A. Search for Encapsulation of Platinum, Silver, and Gold at the Surface of Graphite. *Phys. Rev. Res.* **2020**, *2*, No. 033175.
- (45) Beniwal, S.; Chai, W.; Metavarayuth, K.; Maddumapatabandi, T. D.; Shkaya, D. M.; Henkelman, G.; Chen, D. A. Oxidation of Sn at

- the Cluster-Support Interface: Sn and Pt-Sn Clusters on TiO<sub>2</sub>(110). *J. Phys. Chem. C* **2021**, *125*, 17671–17683.
- (46) Tenney, S. A.; Ratliff, J. S.; He, W.; Roberts, C. C.; Ammal, S. C.; Heyden, A.; Chen, D. A. Adsorbate-Induced Changes in the Surface Composition of Bimetallic Clusters: Au-Pt on TiO<sub>2</sub>(110). *J. Phys. Chem. C* **2010**, *114*, 21652–21663.
- (47) Wahlstrom, E.; Lopez, N.; Schaub, R.; Thostrup, P.; Ronnau, A.; Africh, C.; Laegsgaard, E.; Norskov, J. K.; Besenbacher, F. Bonding of Gold Nanoclusters to Oxygen Vacancies on Rutile TiO<sub>2</sub>(110). *Phys. Rev. Lett.* **2003**, *90*, No. 026101.
- (48) Valden, M.; Lai, X.; Goodman, D. W. Onset of Catalytic Activity of Gold Clusters on Titania with the Appearance of Nonmetallic Properties. *Science* **1998**, *281*, 1647–1650.
- (49) Chen, D. A.; Bartelt, M. C.; McCarty, K. F.; Hwang, R. Q. Self-Limiting Growth of Cu Islands on TiO<sub>2</sub>(110). *Surf. Sci.* **2000**, *450*, 78–97.
- (50) Zhou, J.; Kang, Y. C.; Chen, D. A. Controlling Island Size Distributions: A Comparison of Nickel and Copper Growth on TiO<sub>2</sub>(110). *Surf. Sci.* **2003**, *537*, L429–L434.
- (51) Park, J. B.; Ratliff, J. S.; Ma, S.; Chen, D. A. *In Situ* Scanning Tunneling Microscopy Studies of Bimetallic Cluster Growth: Pt-Rh on TiO<sub>2</sub>(110). *Surf. Sci.* **2006**, *600*, 2913–2923.
- (52) Chen, D. A.; Seutter, S. M.; Bartelt, M. C.; McCarty, K. F. Small, Uniform, and Thermally Stable Silver Particles on TiO<sub>2</sub>(110)-(1 × 1). *Surf. Sci.* **2000**, *464*, L708–L714.
- (53) Jak, M. J. J.; Konstapel, C.; van Kreuningen, A.; Chrost, J.; Verhoeven, J.; Frenken, J. W. M. The Influence of Substrate Defects on the Growth Rate of Palladium Nanoparticles on a TiO<sub>2</sub>(110) Surface. *Surf. Sci.* **2001**, *474*, 28–36.
- (54) Galhenage, R. P.; Yan, H.; Rawal, T. B.; Le, D.; Brandt, A. J.; Maddumapatabandi, T. D.; Nguyen, N.; Rahman, T. S.; Chen, D. A. MoS<sub>2</sub> Nanoclusters Grown on TiO<sub>2</sub>: Evidence for New Adsorption Sites at Edges and Sulfur Vacancies. *J. Phys. Chem. C* **2019**, *123*, 7185–7201.
- (55) Galhenage, R. P.; Xie, K.; Yan, H.; Seuser, G. S.; Chen, D. A. Understanding the Growth, Chemical Activity, and Cluster-Support Interactions for Pt-Re Bimetallic Clusters on TiO<sub>2</sub>(110). *J. Phys. Chem. C* **2016**, *120*, 10866–10878.
- (56) Duke, A. S.; Xie, K.; Brandt, A. J.; Maddumapatabandi, T. D.; Ammal, S. C.; Heyden, A.; Monnier, J. R.; Chen, D. A. Understanding Active Sites in the Water-Gas Shift Reaction for Pt-Re Catalysts on Titania. *ACS Catal.* **2017**, *7*, 2597–2606.
- (57) Duke, A. S.; Xie, K.; Monnier, J. R.; Chen, D. A. Superior Long-Term Activity for a Pt-Re Alloy Compared to Pt in Methanol Oxidation Reactions. *Surf. Sci.* **2017**, *657*, 35–43.
- (58) Galhenage, R. P.; Ammal, S. C.; Yan, H.; Duke, A.; Tenney, S. A.; Heyden, A.; Chen, D. A. Nucleation, Growth and Adsorbate-Induced Changes in Composition for Co-Au Bimetallic Clusters on TiO<sub>2</sub>. *J. Phys. Chem. C* **2012**, *116*, 24616–24629.
- (59) Brandt, A. J.; Maddumapatabandi, T. D.; Shakya, D. M.; Xie, K. M.; Seuser, G. S.; Farzandh, S.; Chen, D. A. Water-Gas Shift Activity on Pt-Re Surfaces and the Role of the Support. *J. Chem. Phys.* **2019**, *151*, No. 234714.
- (60) Park, J. B.; Ratliff, J. S.; Ma, S.; Chen, D. A. Understanding the Reactivity of Oxide-Supported Bimetallic Clusters: Reaction of NO with CO on TiO<sub>2</sub>(110)-Supported Pt-Rh Clusters. *J. Phys. Chem. C* **2007**, *111*, 2165–2176.
- (61) Park, J. B.; Conner, S. F.; Chen, D. A. Bimetallic Pt-Au Clusters on TiO<sub>2</sub>(110): Growth, Surface Composition and Metal-Support Interactions. *J. Phys. Chem. C* **2008**, *112*, 5490–5500.
- (62) Tenney, S. A.; He, W.; Roberts, C. C.; Ratliff, J. S.; Shah, S. I.; Shafai, G. S.; Turkowski, V.; Rahman, T. S.; Chen, D. A. CO-Induced Diffusion of Ni Atoms to the Surface of Ni–Au Clusters on TiO<sub>2</sub>(110). *J. Phys. Chem. C* **2011**, *115*, 11112–11123.
- (63) Ratliff, J. S. The Morphology and Catalytic Activity of Bimetallic Nanoclusters Supported on TiO<sub>2</sub>(110). *Ph.D. Thesis*, University of South Carolina, Columbia, SC, 2009.
- (64) Kresse, G.; Hafner, J. Ab Initio Molecular-Dynamics for Liquid-Metals. *Phys. Rev. B* **1993**, *47*, 558–561.
- (65) Kresse, G.; Hafner, J. Ab Initio Molecular-Dynamics Simulation of the Liquid-Metal Amorphous-Semiconductor Transition in Germanium. *Phys. Rev. B* **1994**, *49*, 14251–14269.
- (66) Kresse, G.; Furthmüller, J. Efficiency of Ab Initio Total Energy Calculations for Metals and Semiconductors Using a Plane-Wave Basis Set. *Comput. Mater. Sci.* **1996**, *6*, 15–50.
- (67) Kresse, G.; Furthmüller, J. Efficient Iterative Schemes for Ab Initio Total-Energy Calculations Using a Plane-Wave Basis Set. *Phys. Rev. B* **1996**, *54*, 11169–11186.
- (68) Kresse, G.; Joubert, D. From Ultrasoft Pseudopotentials to the Projector Augmented-Wave Method. *Phys. Rev. B* **1999**, *59*, 1758–1775.
- (69) Blochl, P. E. Projector Augmented-Wave Method. *Phys. Rev. B* **1994**, *50*, 17953–17979.
- (70) Perdew, J. P.; Burke, K.; Ernzerhof, M. Generalized Gradient Approximation Made Simple. *Phys. Rev. Lett.* **1996**, *77*, 3865–3868.
- (71) Grimme, S. Semiempirical GGA-Type Density Functional Constructed with a Long-Range Dispersion Correction. *J. Comput. Chem.* **2006**, *27*, 1787–1799.
- (72) Henkelman, G.; Uberuaga, B. P.; Jonsson, H. A Climbing Image Nudged Elastic Band Method for Finding Saddle Points and Minimum Energy Paths. *J. Chem. Phys.* **2000**, *113*, 9901–9904.
- (73) Stempel, S.; Bäumer, M.; Freund, H. J. STM Studies of Rhodium Deposits on an Ordered Alumina Film - Resolution and Tip Effects. *Surf. Sci.* **1998**, *402–404*, 424–427.
- (74) Atamny, F.; Baiker, A. Platinum Particles Supported on Carbon: Potential and Limitations of Characterization by STM. *Surf. Interface Anal.* **1999**, *27*, 512–516.
- (75) Atamny, F.; Baiker, A. Investigation of Carbon-Based Catalysts by Scanning Tunneling Microscopy: Opportunities and Limitations. *Appl. Catal. A* **1998**, *173*, 201–230.
- (76) H., G. N. Metallic Carbides. *Nature* **1896**, *54*, 357–357.
- (77) Oden, L. L.; Gokcen, N. A. Sn-C and Al-Sn-C Phase Diagrams and Thermodynamic Properties of C in the Alloys: 1550 to 2300 °C. *Metall. Trans. B* **1993**, *24*, 53–58.
- (78) Slater, J. C. Atomic Radii in Crystals. *J. Chem. Phys.* **1964**, *41*, 3199–3204.
- (79) Brewer, L.; Porter, R. F. The Heat of Sublimation of Tin and the Dissociation Energy of SnO. *J. Chem. Phys.* **1953**, *21*, 2012–2013.
- (80) Hampson, R. F.; Walker, R. F. Vapor Pressures of Platinum, Iridium, and Rhodium. *J. Res. Natl. Bur. Stand.* **1961**, *65A*, 289–295.
- (81) Hampson, R. F.; Walker, R. F. Vapor Pressure of Palladium. *J. Res. Natl. Bur. Stand.* **1962**, *66A*, 177–178.
- (82) Plante, E. R.; Szwarc, R. Vapor Pressure and Heat of Sublimation of Rhenium. *J. Res. Natl. Bur. Stand.* **1966**, *70A*, 175–179.
- (83) Campbell, C. T. Ultrathin Metal Films and Particles on Oxide Surface: Structural, Electronic and Chemisorptive Properties. *Surf. Sci. Rep.* **1997**, *27*, 1–111.
- (84) Rice, C. M.; Eppelsheimer, D. S.; McNeil, M. B. Surface Tension of Solid Tin. *J. Appl. Phys.* **1966**, *37*, 4766–4768.
- (85) Kocherlakota, L. S.; Krajina, B. A.; Overney, R. M. Communication: Local Energetic Analysis of the Interfacial and Surface Energies of Graphene from the Single Layer to Graphite. *J. Chem. Phys.* **2015**, *143*, No. 241105.
- (86) Prudnikova, G. V.; Vjatkin, A. G.; Ermakov, A. V.; Shikin, A. M.; Adamchuk, V. K. Surface Intercalation of Graphite by Lanthanum. *J. Electron Spectrosc. Relat. Phenom.* **1994**, *68*, 427–430.

#### NOTE ADDED AFTER ASAP PUBLICATION

This paper was published ASAP on February 19, 2024, with an error in the caption of Figure 8. The corrected version was reposted with the issue on February 29, 2024.